Matter

Article

Atomic-level etching enables black phosphorus-based electrocatalysts with tuned high-loading single-atom/nanocluster microdomains

Graphical abstract

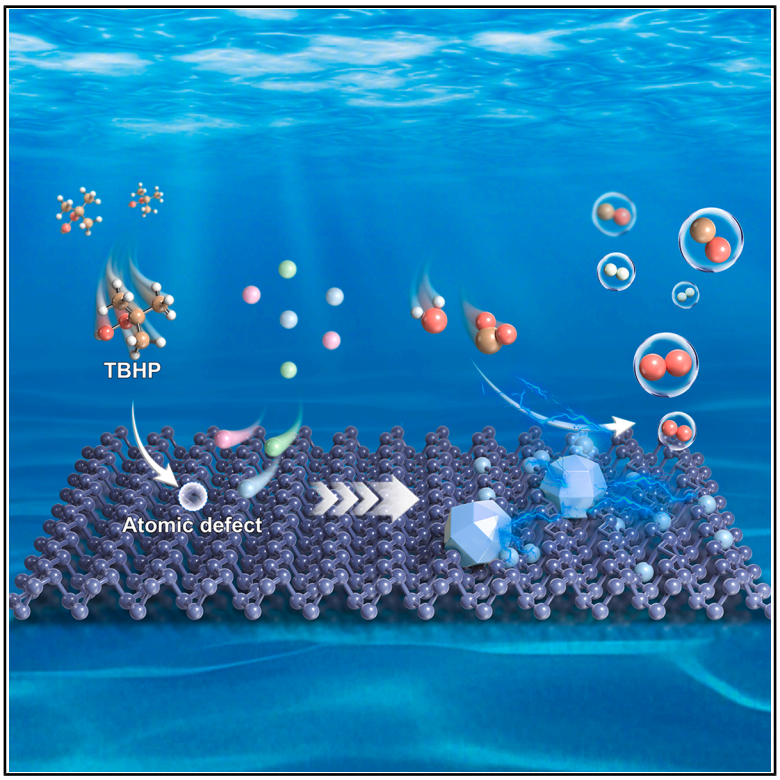

Highlights

- BIAES is proposed to prepare BP NSs with atomic-level defects
- ad-BP NSs guide SA/NC formation through defect anchoring and spatial confinement
- Metal-support interaction and SA-NC synergy promote catalytic reaction

Authors

Yijie Fan, Zhuo Wang, Cong Liu, ..., Zhou Li, Dan Luo, Dingsheng Wang

Correspondence

liucong@binn.cas.cn (C.L.), li_zhou@tsinghua.edu.cn (Z.L.), luodan@binn.cas.cn (D.L.)

In brief

A biphasic interfacial atomic etching strategy (BIAES) is proposed to introduce atomic-scale defects into black phosphorus nanosheets, thereby providing high-density anchoring sites and spatial confinement for controllable loading of metal single atom (SA) /nanocrystal (NC) microdomains. Strong metal-support interactions and NC-induced modulation of adjacent SA sites boost catalytic performance.

Development
Practical, real world, technological considerations and constraints

Fan et al., 2026, Matter 9, 102857
August 5, 2026
https://doi.org/10.1016/j.matt.2026.102857

CellPress

Please cite this article in press as: Fan et al., Atomic-level etching enables black phosphorus-based electrocatalysts with tuned high-loading single-atom/nanocluster microdomains, Matter (2026), https://doi.org/10.1016/j.matt.2026.102857

Matter

CellPress

Article

Atomic-level etching enables black phosphorus-based electrocatalysts with tuned high-loading single-atom/nanocluster microdomains

Yijie Fan,[1,2,3,5] Zhuo Wang,[1,2,3,5] Cong Liu,[1,3,*] Bowen Guo,[1,3] Wen Wang,[1,3] Shenggeng Zhao,[1,3] Jingning Zhang,[1,3] Wei Liu,[1,3] Chang Zhu,[1,3] Kailiang Ren,[1,3] Zhou Li,[4,*] Dan Luo,[1,3,6,*] and Dingsheng Wang[2]

[1]Beijing Institute of Nanoenergy and Nanosystems, Beijing Key Laboratory of High-Entropy Energy Materials and Devices, Chinese Academy of Sciences, Beijing 101400, China

[2]Department of Chemistry, Tsinghua University, Beijing 100084, China

[3]School of Nanoscience and Engineering, University of Chinese Academy of Sciences, Beijing 100049, China

[4]Beijing Tsinghua Changgung Hospital, School of Clinical Medicine, School of Biomedical Engineering, Tsinghua Medicine, Tsinghua University, Beijing 100084, China

[5]These authors contributed equally

[6]Lead contact

*Correspondence: liucong@binn.cas.cn (C.L.), li_zhou@tsinghua.edu.cn (Z.L.), luodan@binn.cas.cn (D.L.)

https://doi.org/10.1016/j.matt.2026.102857

PROGRESS AND POTENTIAL Precisely constructing single-atom and nanocluster (SA/NC) architectures on two-dimensional (2D) carriers has long remained a major challenge in materials synthesis. Despite the large surface area and rich structural tunability of 2D materials, metal species tend to nucleate at high-energy edge sites and subsequently aggregate into larger particles, making it difficult to achieve high loading, uniform dispersion, and precise control over local structures. This study addresses this limitation through a biphasic interfacial atomic etching strategy (BIAES) that generates abundant atomic-scale defect sites on black phosphorus nanosheets (BP NSs). These defects effectively trap metal precursors, confine their local growth, and suppress nanoparticle formation, thereby enabling the high-density coexistence of SAs and NCs.
More importantly, the atomically defective BP NSs prepared by BIAES exhibit universality for metal loading. M-SA/NC@ad-BP (M = Co, Cu, Fe, Ni) are successfully synthesized and demonstrated excellent performance in various catalytic reactions. The superior performance of M-SA/NC@ad-BP arises from the synergistic effect between SA and NC sites, together with strong metal-support interactions. In particular, the NC sites can modulate the local electronic structure of adjacent SA sites, thereby optimizing the adsorption of key reaction intermediates and enhancing catalytic activity. In summary, this study provides new insights into the precise atomic-scale manipulation of the BP interface and the controllable fabrication of SA/NC microdomains.

SUMMARY

Single-atom and nanocluster (SA/NC) catalysts represent the forefront of SA catalysis due to their synergistic catalytic active sites while maintaining exceptional atomic efficiency. However, the intrinsically high surface energy of both SAs and NCs drives their aggregation on carriers, typically resulting in the formation of stable nanoparticles rather than isolated atomic species. In this work, we proposed a biphasic interfacial atomic etching strategy (BIAES) to construct atomically defective black phosphorus nanosheet (ad-BP NS) carriers, enabling the universal high-density loading of metal SAs and NCs on ad-BP NSs (M-SA/NC@ad-BP, M = Co, Fe, Ni, Cu). Experimental and theoretical calculations indicated that the high reactivity and spatial confinement of the atomic-scale defective sites in ad-BP NSs were crucial for the synthesis of M-SA/NC@ad-BP. Strong metal-support interactions, coupled with NC-induced electronic modulation of SA, confer exceptional electrocatalytic activity across multiple reactions. This strategy lays the foundation for the design of high-performance 2D carrier-based SA/NC electrocatalysts.

Please cite this article in press as: Fan et al., Atomic-level etching enables black phosphorus-based electrocatalysts with tuned high-loading single-atom/nanocluster microdomains, Matter (2026), https://doi.org/10.1016/j.matt.2026.102857

INTRODUCTION

The development of single-atom/nanocluster (SA/NC) catalysts has emerged as a groundbreaking frontier in heterogeneous SA catalysis. By providing diverse active sites and high density of reactive centers,[1,2] SA/NC catalysts transcend the inherent limitations of conventional SA catalysts, thereby broadening their potential applicability to complex reactions.[3–5] A notable characteristic of SA/NC catalysts is the coexistence of isolated SAs and NCs on the surface of nanocarriers. Constructing nanocarriers with a spatial structure and chemical environment that favors a balanced and widespread distribution of SA and NC sites is crucial.[6,7] Ideal nanocarriers form strong interfacial coupling between SAs and NCs through robust metal-carrier interactions.[8,9] This not only reduces the high surface free energy of SA and NC to suppress their migration and aggregation but also enables efficient charge-carrier transport and minimizes the interfacial charge transfer barrier. Beyond providing physical stability, carriers also modulate the electronic structure of SAs and NCs,[10] thereby optimizing the adsorption and desorption of key intermediates, enhancing structural stability during catalytic process, and ultimately boosting intrinsic catalytic activity.[3] Therefore, the rational design of carriers with finely tuned physical architectures and chemical properties is critical for the preparation of SA/NC catalysts with high active-site density, structural uniformity, and outstanding performance.

Among the broad range of carriers, two-dimensional (2D) carriers have emerged as ideal platforms for the construction of SA/NC catalysts, owing to their large surface area,[11–13] excellent electrical conductivity, and superior tunability. The unique geometry of 2D carriers provide abundant metal anchor sites, including basal plane, defect, and edge sites[14]; however, the highly unsaturated coordination and high surface energy of edge sites render them prone to serve as primary reduction sites for metal atoms.[15–17] Due to the strong inter-metallic interactions, the energy barrier for metal-metal bonding is typically lower than that for metal-carrier interactions. Consequently, this thermodynamic preference facilitates spontaneous metal coalescence through Ostwald ripening mechanisms at the edges of the 2D nanocarrier, ultimately resulting in the formation of thermodynamically stable nanoparticles rather than isolated atomic species.[18] The kinetic competition between SA stabilization and NC coalescence inherently constrains the achievable SA site densities and uniform spatial distributions. Such morphological evolution not only diminishes metal utilization efficiency via burying active sites, but also alters reaction pathways through size-dependent electronic structure modulation, ultimately leading to a marked decrease in macroscopic catalytic performance. Therefore, it is essential to establish methodologically controllable and structurally adaptable methods that regulate the thermodynamic-kinetic balance between metal-metal versus metal-carrier bonding energetics, realizing the SA/NC catalysts on 2D nanocarriers with high active-site dispersion and structural uniformity.

In the present study, we proposed a biphasic interfacial atomic etching strategy (BIAES) to modify 2D black phosphorus nanosheets (BP NSs) to create a high density of atomic-scale defects on their surfaces, ultimately enabling the uniform, abundant, and universal loading of various metal-based SAs and NCs onto the surfaces of atomically defective BP NSs (ad-BP NSs). Specifically, the atomic-scale defects generated by BIAES modification served as anchoring sites for the metal precursors, enhancing the interaction between the support and the metal precursors. Simultaneously, they also provided confined spaces, stabilizing the metal active centers and improving their dispersion while suppressing nanoparticle crystallization to maintain high atomic efficiency. Using BIAES-treated ad-BP NSs as nanocarriers, we conveniently synthesized a cobalt (Co)-based electrocatalyst uniformly loaded with SA and NC on the ad-BP surface (Co-SA/NC@ad-BP) via a solvothermal method. In contrast, when BP NSs were used as nanocarriers, the Co precursor was reduced to form larger nanoparticles (>3 nm in size) that were primarily deposited at the edges of the NSs (eg-Co NP@BP), with only a small portion of SA and NC loaded on the BP NSs surface. X-ray absorption spectroscopy (XAS) and DFT calculations revealed that Co-based SA components (Co SAs) served as the primary active site during the OER. The strong interactions between Co SAs, Co_2P NCs (Co_2P NCs), and the BP-based nanocarrier significantly enhanced electron transfer during the catalytic process. Co_2P NC could further modulate the adsorption energy of the reaction intermediate O* on Co SA by influencing its electronic structure, thereby enhancing the overall activity of the catalyst. This synthetic strategy can also be extended to the synthesis of other transition metal-based SA/NC catalysts, including Cu, Fe, and Ni, which have demonstrated remarkable activity in various electrocatalytic applications. The BIAES strategy provides new insights into the optimization of 2D carriers and is expected to enable the precise synthesis of SA/NC catalysts with well-defined structures and targeted functionalities.

RESULTS AND DISCUSSION

Synthesis and characterization of ad-BP NSs

First, BP NSs were synthesized via ultrasonic liquid-phase exfoliation in N-methylpyrrolidone (NMP).[19] Then, ad-BP NSs were prepared via BIAES, as shown in Figure 1A and Figure S1. The process of BIAES occurs at the interface between decane and water, where *tert*-butyl hydroperoxide dissolved in the decane phase serves as the oxidant, while BP NSs are dispersed in the aqueous phase. Under gentle stirring, an interfacial oxidation reaction takes place in which *tert*-butyl hydroperoxide reacts with surface phosphorus (P) atoms on the BP NSs, forming phosphorus oxides. Subsequently, the interaction with water molecules removes the oxidized P atoms, resulting in the formation of atomic-level defects.[20] Transmission electron microscopy (TEM) and atomic force microscopy (AFM) images confirmed the lamellar structure of BP NSs (Figures 1B and 1D).[19] Discrete diffraction spots observed in the selected area electron diffraction (SAED) pattern (Figure S2) correspond to the (040), (041), and (042) crystal planes of BP. After moderate *tert*-butyl hydroperoxide etching, the morphology of BP NSs remains largely unchanged (Figures 1E and S3), whereas excessive etching leads to increased defect density and compromised lattice stability (Figure S4). To visualize the presence of P vacancies, aberration-corrected high-angle annular dark-field scanning TEM

Please cite this article in press as: Fan et al., Atomic-level etching enables black phosphorus-based electrocatalysts with tuned high-loading single-atom/nanocluster microdomains, Matter (2026), https://doi.org/10.1016/j.matt.2026.102857

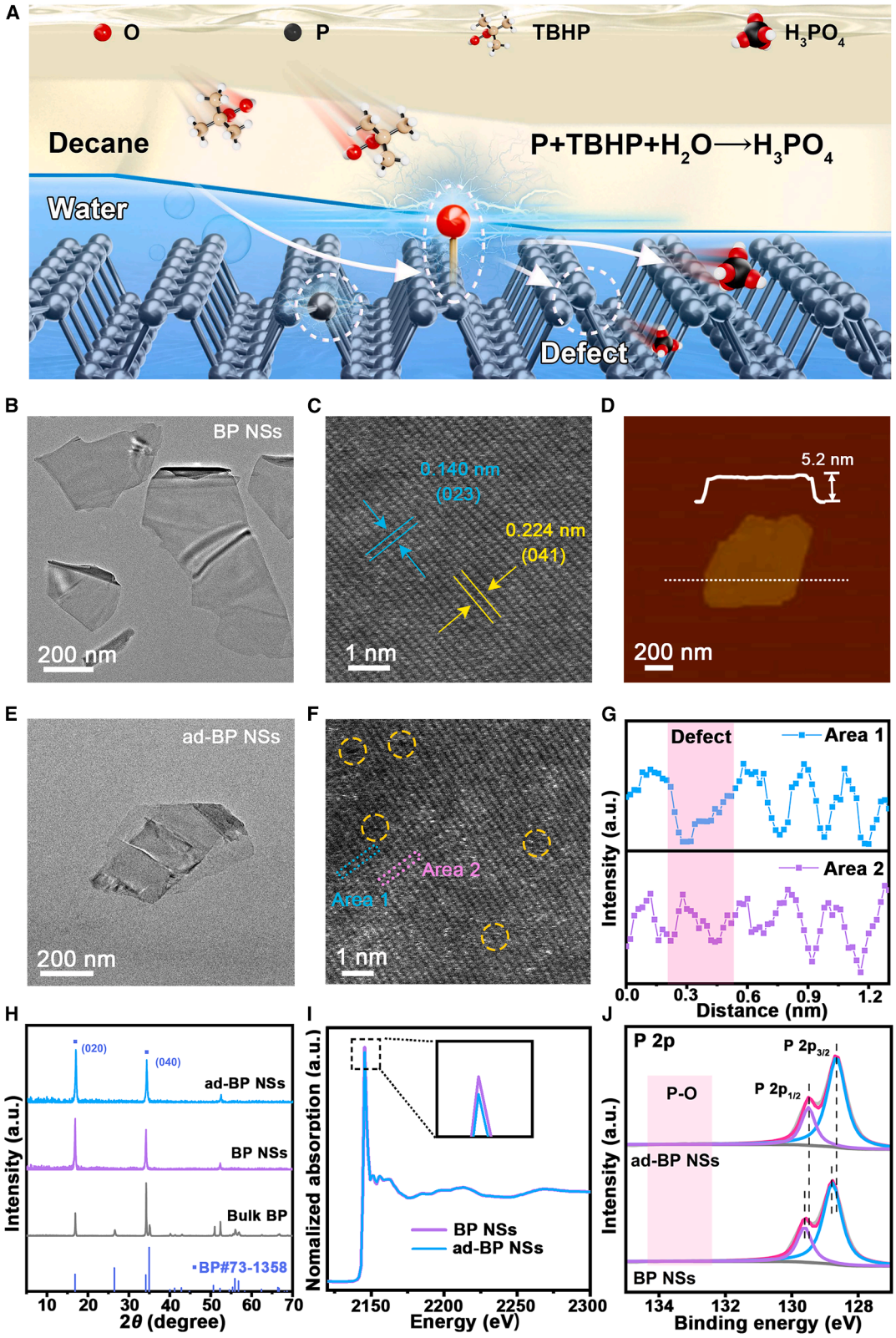

(legend on next page)

Please cite this article in press as: Fan et al., Atomic-level etching enables black phosphorus-based electrocatalysts with tuned high-loading single-atom/nanocluster microdomains, Matter (2026), https://doi.org/10.1016/j.matt.2026.102857

(AC-HAADF-STEM) was performed on pristine and ad-BP NSs. In the pristine state, the AC-HAADF-STEM images revealed a defect-free, highly ordered atomic arrangement, with interplanar spacing corresponding to the (023) and (041) crystal planes of BP (Figure 1C). In contrast, ad-BP NSs exhibited isolated P vacancies and few adjacent P vacancies on the surface (Figure 1F). The presence of P vacancies was further confirmed by the intensity profile along the dotted box in Figure 1G.[21,22] The evolution of Raman spectra from bulk BP to ad-BP NSs is shown in Figure S5. The Raman spectrum of bulk BP exhibits three characteristic peaks corresponding to one out-of-plane phonon mode (A_g^1) and two in-plane modes (B_{2g} and A_g^2). Notably, all peaks in BP NSs and ad-BP NSs shift slightly toward higher wavenumbers compared to bulk BP, confirming that ad-BP NSs retain fine crystallinity. Consistently, XRD spectra display sharp diffraction peaks corresponding to the (040) and (020) crystal planes of BP, further supporting the above conclusion (Figure 1H). Meanwhile, X-ray photoelectron spectroscopy (XPS) analysis shows no significant increase in the P–O ratio, indicating that defect formation is confined to localized atomic-scale etching rather than bulk oxidation (Figure 1J).

To further investigate the surface composition and coordination environment of ad-BP NSs, X-ray absorption near-edge structure (XANES) and XPS analyses were performed. Both BP NSs and ad-BP NSs exhibit typical XANES spectra with identical edge positions and comparable white line intensities (Figure 1I). Specifically, the white line peak (P(0)) at approximately 2,145.5 eV corresponds to the electronic transition from the P 1s orbital to the unoccupied electronic states of P 3p character. The peaks at 2,151.4 and 2,155.9 eV are attributed to higher oxidation states, specifically P(III) and P(V), respectively. Compared to pristine BP NSs, ad-BP NSs show only a slight increase in the P(V) peak,[23] indicating that the BIAES minimally affects the oxidation state of the BP NSs. In addition, the intensity of the P(0) peak is slightly decreased, which might be due to the P vacancies generated after biphasic interfacial atomic etching. The P 2p XPS spectra in Figure 1J reveal that the P $2p_{3/2}$ peak of ad-BP NSs shifts from 128.8 to 128.7 eV, while the P $2p_{1/2}$ peak shifts from 129.6 to 129.5 eV. These changes further indicate the presence of P vacancies in the ad-BP NSs.[24,25]

Synthesis and structural characterization of Co-SA/NC@ad-BP

In the catalytic reactions, the amount of loaded metal typically has a direct impact on the catalyst's activity. However, excessive metal loading can result in particle aggregation, diminishing catalytic performance. Therefore, designing electrocatalysts with both high activity and excellent metal dispersion is of paramount importance. Here, we developed a general solvothermal synthesis method using BIAES-treated ad-BP NSs as the nanocarrier. The formation mechanism of Co-SA/NC@ad-BP is illustrated in Figure 2A. During the liquid-phase exfoliation process, BP NSs inevitably develop defects due to transverse fractures.[26] Defect regions have unsaturated coordination environments and tend to serve as active sites for synthesis/catalytic reactions.[27] As most defects form at the edge positions during exfoliation, metal precursor reduction primarily occurs at the edges, leading to suboptimal utilization of the surface of the BP NSs. When BP NSs were utilized as nanocarriers for electrocatalyst synthesis, Co atoms were predominantly reduced to form Co_2P NPs at the edge regions of NSs (Figure 2B). This is likely due to the higher concentration of P vacancies at the edges, where reduced spatial constraints facilitate the reduction process. High-resolution TEM (HR-TEM) revealed a lattice spacing of 0.220 nm at the edges, corresponding to the (111) crystallographic plane of Co_2P, while the typical (111) crystallographic plane of BP was observed in the central regions of NSs (Figures S6A–S6C). The AC-HAADF-STEM images further showed that Co_2P was predominantly distributed at the edge regions (Figures 2D and 2E), with only a small amount of Co SAs and Co_2P NCs present on the NS surfaces. Energy-dispersive X-ray spectroscopy (EDS) mapping (Figure 2C) and Co element line scans (Figures S7A and S7B) corroborated the above results. In contrast, when ad-BP NSs were employed for electrocatalyst synthesis, Co atoms were uniformly distributed across the NS surfaces rather than being primarily concentrated at the edges (Figures 2F, 2G, S7C, and S7D). HR-TEM and AC-HAADF-STEM imaging revealed a dense and uniform distribution of Co_2P NCs (Figures 2H and S6d–S6f). Local magnification further confirmed the coexistence of Co in the form of Co SAs (highlighted by yellow circles) and Co_2P NCs (highlighted by red circles), both evenly distributed on the NS surfaces (Figure 2I). These findings align with the TEM results and confirm the effectiveness of BIAES. The elemental composition of catalysts was examined using XPS, revealing a significant increase in Co atomic content from 26.8 at% in eg-Co NP@BP to 34.2 at% in Co-SA/NC@ad-BP (Figure 2J; Table S1). Statistical analysis of HAADF-STEM images shows that the number of Co SAs in Co-SA/NC@ad-BP increased by 9.7 times compared to eg-Co NP@BP. The number of NCs increased by 4.2 times, while the number of NPs showed a significant decrease (Figures 2K–2M). These findings suggest that the BIAES alters the distribution of Co atoms on the surface of BP NSs and enhances the Co loading. The crystal structures of eg-Co NP@BP and

Figure 1. Synthesis and structural characterizations of ad-BP NSs

(A) Schematic illustration of the ad-BP NSs synthesis.
(B) TEM images of BP NSs.
(C) AC-HAADF-STEM image of BP NSs.
(D) AFM images of BP NSs.
(E) TEM images of ad-BP NSs.
(F) AC-HAADF-STEM image of ad-BP NSs.
(G) The corresponding intensity profile of the defect BP NSs along the dashed rectangles, showing the isolated arrangement of P atoms.
(H) XRD patterns of bulk BP, BP NSs, and ad-BP NSs.
(I) Normalized P K-edge XANES spectra of BP NSs and ad-BP NSs.
(J) P 2p XPS spectra and curve fitting result of BP NSs and ad-BP NSs.

Please cite this article in press as: Fan et al., Atomic-level etching enables black phosphorus-based electrocatalysts with tuned high-loading single-atom/nanocluster microdomains, Matter (2026), https://doi.org/10.1016/j.matt.2026.102857

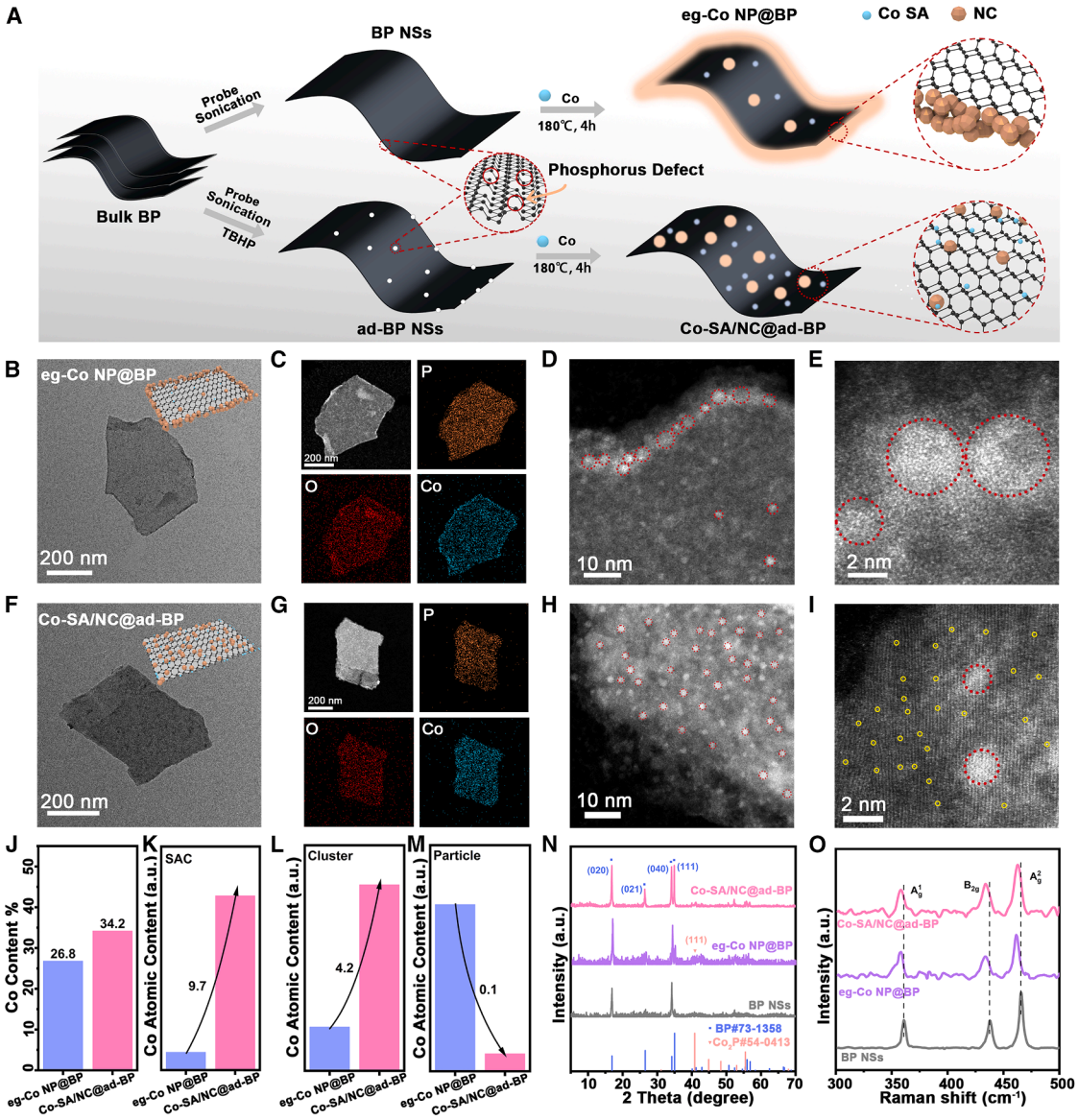

Figure 2. Synthesis and structural characterizations of catalysts

(A) Schematic illustration of the Co-SA/NC@ad-BP and eg-Co NP@BP synthesis process.
(B) TEM image of eg-Co NP@BP.
(C) EDS mapping images of eg-Co NP@BP, showing the distribution of P, O, and Co.
(D and E) AC-HAADF-STEM image under low and high magnitudes of eg-Co NP@BP.
(F) TEM image of Co-SA/NC@ad-BP.
(G) EDS mapping images of Co-SA/NC@ad-BP, showing the distribution of the P, O, and Co.
(H and I) AC-HAADF-STEM image under low and high magnitudes of Co-SA/NC@ad-BP.
(J) Co atomic proportion of eg-Co NP@BP and Co-SA/NC@ad-BP. Statistical analysis of the relative number of (K) Co SACs, (L) NC, and (M) NP in eg-Co NP@BP and Co-SA/NC@ad-BP derived from HAADF-STEM images.
(N) XRD patterns of Co-SA/NC@ad-BP, eg-Co NP@BP, and BP NSs.
(O) Raman scattering spectra of the Co-SA/NC@ad-BP and eg-Co NP@BP.

Co-SA/NC@ad-BP were characterized by XRD. As shown in Figure 2N, no diffraction peaks corresponding to Co_2P NCs were observed in Co-SA/NC@ad-BP, likely due to their small size. The prominent diffraction peaks were attributed exclusively to BP crystals. Furthermore, the A_g^1, B_{2g}, and A_g^2 vibrational modes in Co-SA/NC@ad-BP were suppressed when Co SAs and Co_2P NCs formed on the ad-BP NSs. This suppression caused a shift of the Co-SA/NC@ad-BP peaks toward lower wavenumbers compared to BP NSs, indicating a strong electronic interaction between the SA/NC and ad-BP NSs (Figure 2O).

Please cite this article in press as: Fan et al., Atomic-level etching enables black phosphorus-based electrocatalysts with tuned high-loading single-atom/nanocluster microdomains, Matter (2026), https://doi.org/10.1016/j.matt.2026.102857

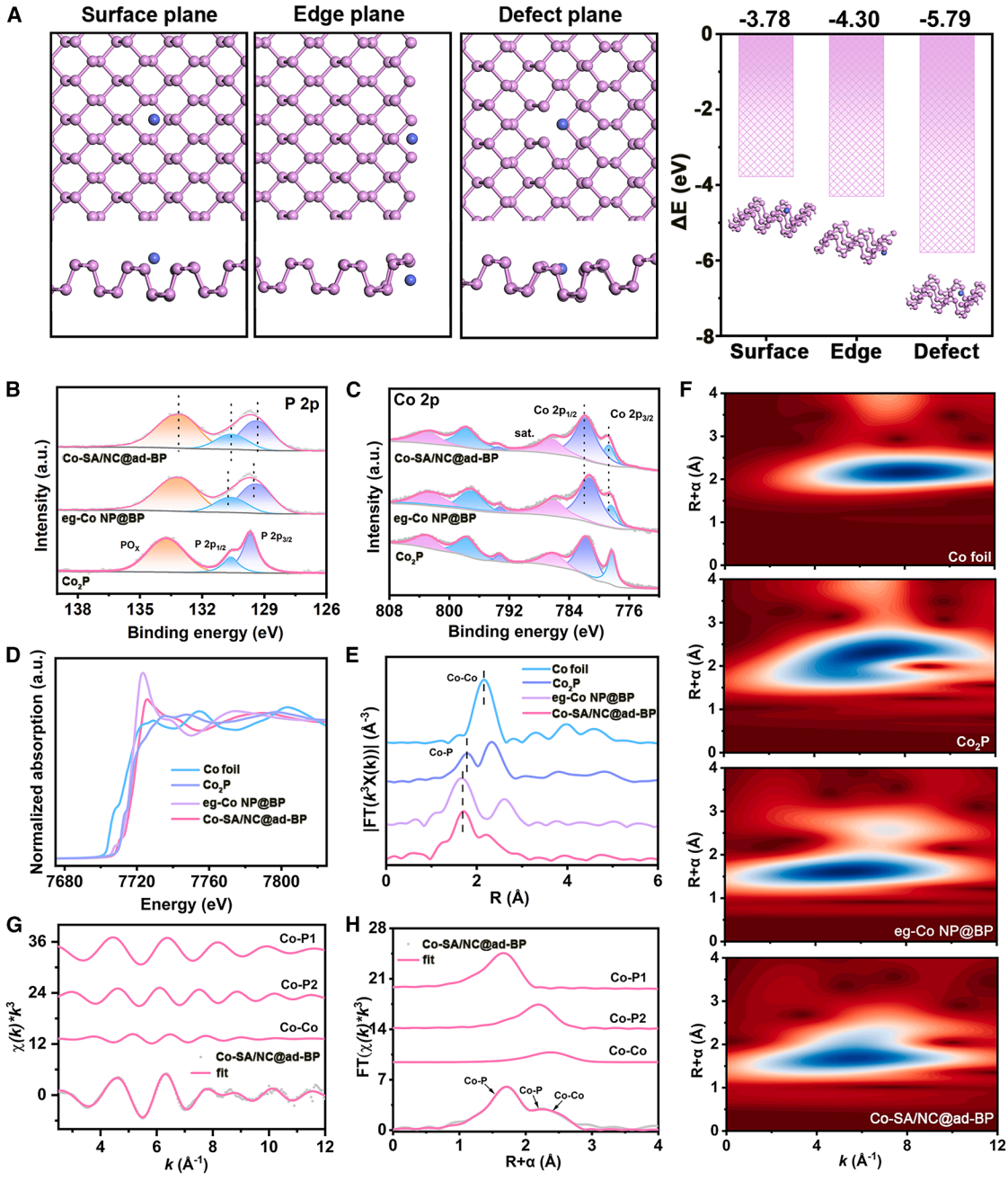

Figure 3. Atomic structure analysis of catalysts

(A–F) (A) Structure model and adsorption energy of Co atoms at different sites (surface, edge and defect sites) of BP NSs. XPS spectra of (B) P 2p, and (C) Co 2p for Co_2P, eg-Co NP@BP and Co-SA/NC@ad-BP, respectively. Normalized Co K-edge XANES spectra (D), Fourier transform k^3-weighted Co K-edge EXAFS spectra (E) and Wavelet transform (F) of Co foil, Co_2P, eg-Co NP@BP, and Co-SA/NC@ad-BP.

(G) Co K-edge EXAFS (points) and the curve-fit (line) for Co-SA/NC@ad-BP, shown in k^3-weighted k-space.

(H) The corresponding EXAFS fitting curves of Co-SA/NC@ad-BP at R-space.

Electronic structure and coordination environment of Co-SA/NC@ad-BP

To elucidate the reduction mechanism of Co atoms, we calculated their adsorption energies on the surface, edges, and defect sites of BP NSs using DFT. The results revealed that the adsorption energies at edge defects (−4.30 eV) and surface defects (−5.79 eV) were significantly lower than that on the pristine BP NSs surface (−3.78 eV) (Figure 3A), indicating a preferential reduction of Co atoms at defect sites. Owing to the size- and space-confining effects of the surface defects, Co atoms are

reduced to SA or NC, effectively preventing their overgrowth into NP. The chemical state and electronic structure of Co-SA/NC@ad-BP were investigated by XPS analysis. The high-resolution XPS spectra of the Co 2p and P 2P regions in Co-SA/NC@ad-BP, as shown in Figures 3B and 3C, exhibit clear spin-orbit coupling, resulting in the splitting of $2p_{3/2}$ and $2p_{1/2}$ doublets. In the P 2p spectra (Figure 3B), two unchanged peaks at 129.5 and 130.7 eV confirm the pristine state of BP,[28] while the oxidation peak at 133.2 eV is likely due to surface contact with atmospheric oxygen.[26,29,30] In the Co 2p spectra (Figure 3C), the Co $2p_{3/2}$ and $2p_{1/2}$ peaks are located at 778.6 and 781.9 eV, respectively, with a satellite peak observed at 786.6 eV. The Co 2p binding energy lies between those characteristics of metallic and oxidized states, confirming the formation of Co_2P NCs. This observation is consistent with previously reported results, further corroborating the successful synthesis of Co_2P.[26] Compared to Co_2P, the Co 2p peak of Co-SA/NC@ad-BP shifts to higher binding energy, accompanied by a corresponding shift of the P 2p peak to lower binding energy, evidencing charge redistribution. This originates from strong interactions between SA/NC and the ad-BP NSs.[31] Furthermore, comparisons with Co SA@BP and Co NC@BP shows that the Co 2p binding energy of Co-SA/NC@ad-BP lies intermediate between the two (Figures S8 and S9),[32,33] indicating modulation of the local electronic environment of Co SAs by NC incorporation. These observations reveal strong electronic coupling between SA and NC.

The electronic structure and coordination environment of Co-SA/NC@ad-BP were investigated using XAS. The primary peaks in the 3d-K edge spectra represent unoccupied 4p states, with their energy positions and shapes predominantly influenced by the crystal structure. The valence state of the 3d element can be determined by analyzing the energy position of the absorption edge.[34] As shown in Figure 3D, the normalized Co K-edge XANES spectrum of Co-SA/NC@ad-BP reveal that the valence state of Co in Co-SA/NC@ad-BP is slightly higher than that of Co_2P. This aligns well with the XPS results. The Co K-edge extended X-ray absorption fine structure (EXAFS) analysis of Co-SA/NC@ad-BP reveals two distinct peaks in R-space. The first peak is clearly attributed to Co–P bonds (Figures 3E and S10).[34] However, the second-shell peak cannot be directly distinguished due to the similar bond lengths of Co-Co in Co foil and Co_2P. The wavelet transforms (WT) EXAFS spectra can directly reflect the structure information in the resolution of R-space and k-space.[35,36] For Co-SA/NC@ad-BP, the first shell domain exhibits a local maximum at approximately 1.7 Å in R-space and 5.2 $Å^{-1}$ in k-space, while the second shell domain shows a maximum near 2.2 Å in R-space and 6.2 $Å^{-1}$ in k-space. Although the R value of the second shell domain in Co foil is similar to the Co–Co scattering in Co-SA/NC@ad-BP (R = 2.2 Å), their k values differ significantly (Co foil: k = 7.9 $Å^{-1}$; Co-SA/NC@ad-BP: k = 6.2 $Å^{-1}$). However, the Co–Co scattering in Co-SA/NC@ad-BP resembles that of Co_2P (R = 2.3 Å and k = 6.6 $Å^{-1}$) (Figure 3F). Notably, the peak position in Co-SA/NC@ad-BP slightly shifts compared to Co_2P, likely due to strong interactions between Co SA/Co_2P NC embedded in the defects and ad-BP NSs carrier. These interactions could induce compression of both Co–P and Co–Co bonds.[37] EXAFS fitting provided further insights into the coordination structure of Co-SA/NC@ad-BP. The EXAFS spectra were analyzed using three coordination paths: Co–P1, Co–P2, and Co–Co (Figures 3G and 3H; Table S2). The fitting results revealed that the primary peak in the first coordination shell domain at 1.7 Å originates from Co–P1 bonds, while the secondary shell domain peak at 2.3 Å is attributed to contributions from Co–P2 (2.2 Å) and Co–Co (2.4 Å) bonds. The coordination number of the first shell domain for Co in Co-SA/NC@ad-BP was determined to be 3.7, compared to approximately 1 for Co_2P (Figure S11). This difference suggests that the first shell coordination in Co-SA/NC@ad-BP arises from a combined contribution of Co SAs and Co_2P NCs.

Electrocatalysis performance of Co-SA/NC@ad-BP

The electrocatalytic OER performance of Co-SA/NC@ad-BP was evaluated using linear sweep voltammetry (LSV) in alkaline media (1.0 M KOH). For comparison, commercial IrO_2, BP NSs, Co_2P, eg-Co NP@BP, SAC@C, NC@C, Co SA@BP, and Co NC@BP were also tested. All the data presented were referenced to the reversible hydrogen electrode (RHE) without iR compensation, where i is the current and R is the uncompensated resistance, and the mass of catalyst loaded on each electrode was kept consistent across all samples. As shown in Figures 4A and 4B, BP NSs displayed negligible OER activity, and the other control catalysts, including Co_2P, eg-Co NP@BP, SAC@C, and NC@C, Co SA@BP, and Co NC@BP (Figures S12–S14), also delivered similarly poor performance. In stark contrast, Co-SA/NC@ad-BP exhibits markedly enhanced activity, requiring a overpotential of only 223 mV at 10 mA cm^{-2}. Its overpotential is substantially lower than those of Co SA@BP and Co NC@BP, confirming a synergistic interaction between SAs and NCs. Furthermore, Co-SA/NC@ad-BP outperformed IrO_2 catalysts at higher current densities (e.g., 50 mA cm^{-2}), underscoring its superior OER performance. Co-SA/NC@ad-BP delivers a Tafel slope of 51 mV dec^{-1}, considerably lower than those of Co_2P, eg-Co NP@BP, SAC@C, NC@C, Co SA@BP, and Co NC@BP, indicating its superior OER activity. This result suggests that the OER kinetic of Co-SA/NC@ad-BP is significantly accelerated (Figure 4C). Additionally, Figure 4D illustrates the advantages of Co-SA/NC@ad-BP, including its low overpotential and smaller Tafel slope, which surpass those of most reported transition metal OER electrocatalysts utilizing BP carriers (Table S3). The evaluation of an electrocatalyst system typically involves two key metrics: specific activity and TOF.[38] To assess these, the double-layer capacitance (C_{dl}) in the non-Faradaic potential region was measured to estimate the electrochemically active surface area (ECSA).[39] As shown in Figures 4E and S15, Co-SA/NC@ad-BP exhibited the highest C_{dl} value (50.3 mF cm^{-2}), compared with eg-Co NP@BP (38.0 mF cm^{-2}) and Co_2P (9.2 mF cm^{-2}). Additionally, Co-SA/NC@ad-BP demonstrated a superior TOF of 0.13 s^{-1} per Co site at 300 mV, reflecting its excellent intrinsic activity (Figure 4F). Remarkably, Co-SA/NC@ad-BP achieved a mass activity (MA) of 0.86 A mg^{-1} at 300 mV, which is 10.4 and 36.7 times higher than those of IrO_2 and eg-Co NP@BP, respectively (Figure 4G). Hence, Co-SA/NC@ad-BP utilizes abundant transition metals to deliver OER performance comparable to noble metal catalysts, highlighting its significant economic advantages. Electrochemical impedance spectroscopy (EIS) was conducted on five samples under

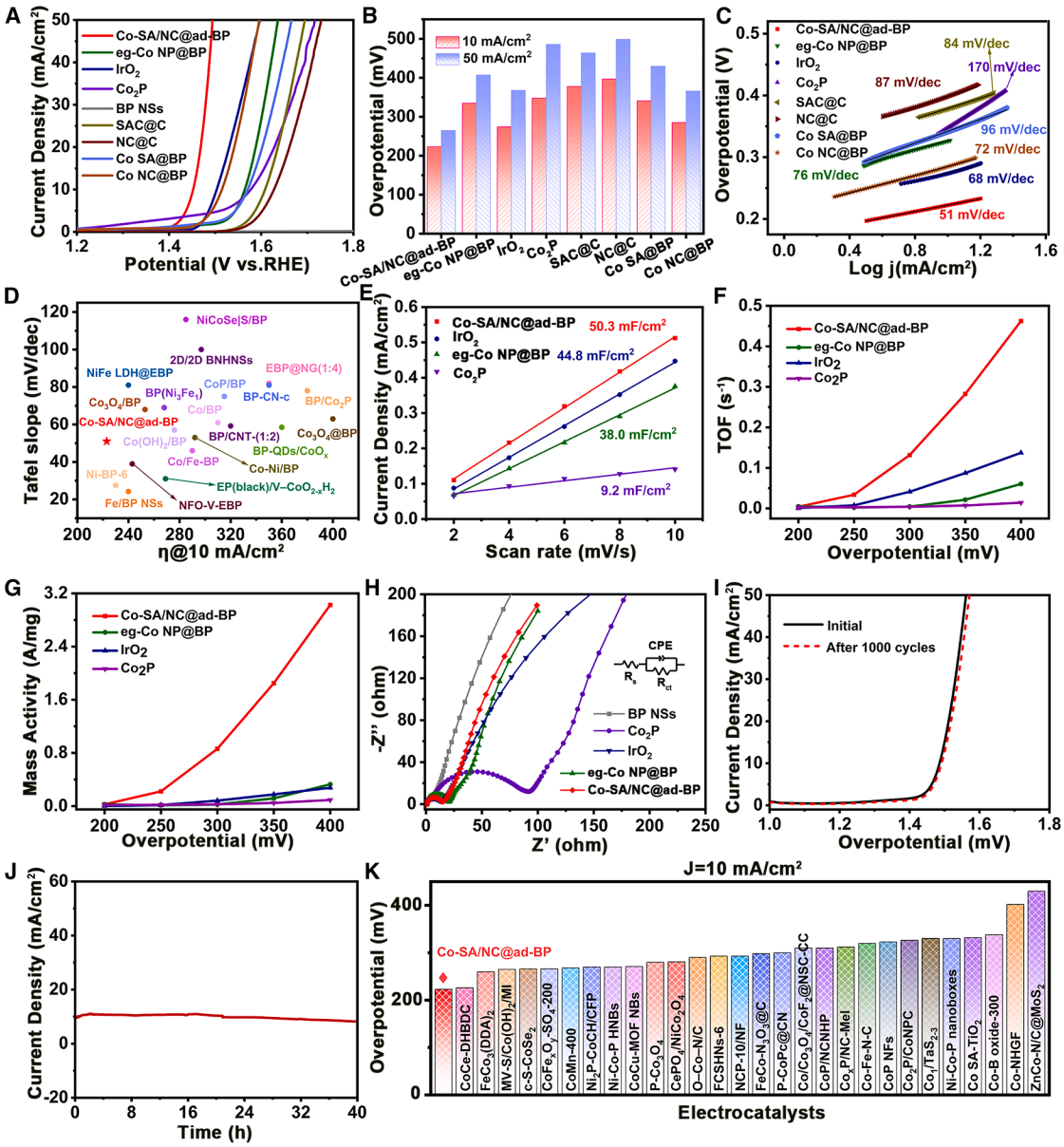

Figure 4. OER performance of catalysts in the three-electrode setup

(A) OER polarization curves of Co-SA/NC@ad-BP, eg-Co NP@BP, IrO_2, Co_2P, BP NSs, SAC@C, NC@C, Co SA@BP, and Co NC@BP in 1.0 M KOH.

(B) The overpotential at 10 and 50 mA cm^{-2}.

(C) Tafel plots originated from LSV curves.

(D) Comparison of the OER performance between Co-SA/NC@ad-BP and those previously reported BP-based catalysts based on kinetics (Tafel slope) and activity (the overpotential at 10 mA cm^{-2}).

(E) Linear fitting of current density as a function of the scan rate.

(F) TOF values at the different overpotential.

(G) MAs at the different overpotential.

(H) EIS Nyquist plots of Co-SA/NC@ad-BP, eg-Co NP@BP, IrO_2, Co_2P, and BP NSs.

(I) The polarization curves of Co-SA/NC@ad-BP after 1,000 CV cycles.

(J) I-t chronoamperometric curves of the Co-SA/NC@ad-BP at 10 mA cm^{-2}.

(K) Comparison of the OER activity between Co-SA/NC@ad-BP with those previously reported Co-based catalysts, originating from Table S4.

identical conditions, and the results are presented in Figure 4H. By constructing equivalent circuits and fitting the Nyquist plots, the charge transfer resistance (R_{ct}) values were determined. Co-SA/NC@ad-BP exhibited the lowest R_{ct} of 13.44 Ω, significantly smaller than those of eg-Co NP@BP, Co_2P, and BP NSs. This result highlights the superior charge transfer efficiency of Co-SA/NC@ad-BP during the OER process.[40] Stability is a critical metric for evaluating OER performance. To assess this, continuous cyclic voltammetry (CV) was conducted in the potential range of 1.22–1.32 V versus RHE at room temperature with a scan rate of 10 mV s^{-1}. As shown in Figure 4I, the LSV polarization curves of Co-SA/NC@ad-BP remained nearly unchanged after 1,000 cycles, with no significant shift observed at a current density of 50 mA cm^{-2}, indicating exceptional stability during continuous CV testing. Furthermore, a constant potential test confirmed the stability of Co-SA/NC@ad-BP, maintaining stable performance for nearly 40 h at a current density of 10 mA cm^{-2} (Figure 4J). Post-reaction structural characterizations reveal that the overall architecture of Co-SA/NC@ad-BP is well preserved under OER conditions, evidencing the structural robustness of the catalyst (Figure S16). A comparison of the overpotential values at 10 mA cm^{-2} showed that Co-SA/NC@ad-BP outperformed most previously reported Co-based catalysts in alkaline solution (Figure 4K). These results suggest that the enhanced catalytic performance of Co-SA/NC@ad-BP originates from the synergistic interaction between SAs and NCs, which modulates the electronic structure and facilitates charge transfer, together with the high dispersion of Co species at elevated loading.

Mechanistic insights into the outstanding OER activity of Co-SA/NC@ad-BP

To investigate the potential catalytic mechanism of OER, a theoretical study based on DFT calculations was conducted. For simplification, the catalyst was assumed to be charge-neutral, and solvent effects were not considered.[41,42] It is widely acknowledged that an ideal OER catalyst must exhibit optimal adsorption strengths for oxygen-containing intermediates at each key step to ensure reaction continuity and efficiency. The schematic atomic structure of the Co-SA/NC@ad-BP and the corresponding optimized adsorption configurations for reactive intermediates (OH*, O*, OOH*, and O_2) are presented in Figures S17 and 5A. The calculated free energies for each OER step are shown in Figure 5B. BP NSs exhibit excessively weak adsorption energies for OOH*-containing intermediates, which hinder catalytic efficiency. Among the five structural models evaluated, the adsorption of O* emerges as the potential rate-determining step. A comparative analysis of the adsorption strengths of Co SA and Co_2P NC at each critical step reveals that the free energy change at the rate-determining step for Co-SA/NC@ad-BP (SA site) is smaller than that for Co SA@BP, Co NC@BP, and Co-SA/NC@ad-BP (NC site). This suggests that Co-SA/NC@ad-BP (SA site) is more thermodynamically favorable. Additionally, the free energy difference for the adsorption step of OOH* at 1.23 V potential for Co-SA/NC@ad-BP (SA site) is 1.56 eV, the lowest among all samples, indicating the smallest adsorption energy barrier for OOH*. These findings demonstrate that the Co SA site serves as the primary catalytic center, while the Co_2P NC plays a crucial role in enhancing the catalytic performance of Co SA.

To further elucidate the structural advantages of Co-SA/NC@ad-BP and the mechanisms underlying its enhanced OER activity, we examined the atomic orbital electronic properties of Co SA@BP and Co-SA/NC@ad-BP. The charge density difference presented in Figure 5C indicates a strong electronic coupling between Co_2P NC and Co SA. The presence of Co_2P NC induces charge redistribution of Co SA, driving the Co SA into an electron-rich state and consequently modifying Co SA adsorption behavior toward oxygenated intermediates (Figure 5C).[43,44] The Co *d*-band center of Co SA@BP is positioned at −1.193 eV (Figures 5D and 5F), whereas that of Co-SA/NC@ad-BP shifts to −1.646 eV, aligning closely with the free energy trends presented in Figure 5B. According to *d*-band theory, a *d*-band center closer to the Fermi energy results in a stronger Co–O bond, enhancing adsorption of intermediates. As Sabatier's principle, an excessive upward shift of the Co *d*-band center relative to the Fermi energy reduces catalytic activity. Furthermore, the charge density of Co-SA/NC@ad-BP near the Fermi level is higher than that of Co AC@BP, thus enhancing electron transfer during the reaction (Figure 5D).[45] Bader charge analysis reveals that approximately 0.20 |e| electrons from the Co SA sites in Co SA@BP are transferred to the BP carrier (Figure 5E). In contrast, with the introduction of Co_2P NC, the number of transferred from Co SA in Co-SA/NC@ad-BP electrons decrease slightly to 0.18 |e|, bringing the adsorption energy of Co SA with O* closer to the ideal state. Thus, the outstanding catalytic performance of Co-SA/NC@ad-BP can be attributed to the synergistic interaction between Co_2P NC and Co SA, which promotes efficient electron redistribution at the Co SA, as well as the strong interaction between Co SA, Co_2P NC, and the BP carrier.

Universal synthesis of M-SA/NC@ad-BP

Building on the insights gained, Figure 6A illustrates the general synthesis pathway for ad-BP NSs-based SA/NC electrocatalysts. The uniform dispersion of SA/NC structures on the BP nanocarrier is heavily influenced by the binding energies of metal precursors to different regions of the carrier. To optimize the synthesis process, DFT calculations were employed to evaluate the binding energies of various metal precursors to different sites on the BP nanocarrier, providing crucial guidance for the formation of uniformly distributed SA/NC electrocatalysts. Calculations indicate that Cu, Fe, and Ni ions exhibit minimal binding energies at defect sites (Figure S18), suggesting that the BIAES for constructing SA/NC electrocatalysts is broadly applicable to these metals. Building upon this, we further investigated the formation mechanism of the SA/NC structures. DFT calculations indicate that the formation of SAs and NCs is governed by the structural characteristics and spatial distribution of phosphorus vacancies (Figure S19). Isolated vacancies exhibit strong metal anchoring capability, stabilizing individual metal atoms as dispersed SA sites. In contrast, spatially adjacent vacancies promote metal-metal interactions, thereby driving NC formation. Both SA and NC configurations are thermodynamically accessible, with the preferred structure determined by the local defect environment. As the etching depth increases, the defect density correspondingly rises, driving structural evolution toward the coexistence of SAs and NCs.

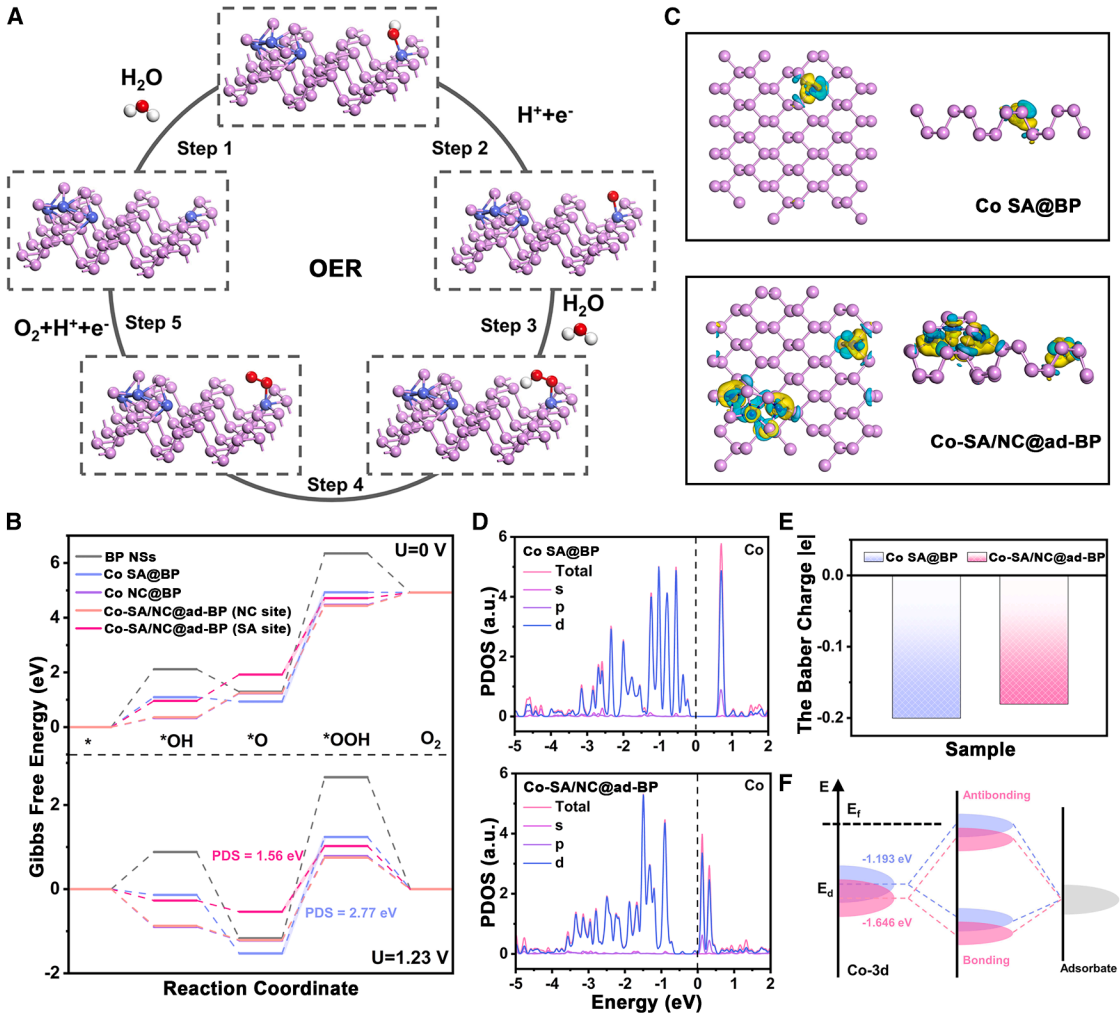

Figure 5. OER mechanism of Co-SA/NC@ad-BP

(A) The proposed OER reaction pathway on Co-SA/NC@ad-BP model.

(B) The Gibbs free energy diagrams of the OER process on the Co sites of catalysts.

(C) Differential charge density of Co SA@BP and Co-SA/NC@ad-BP (the colors yellow and blue represent the increase and decrease of charge density, respectively).

(D) Projected density of states (PDOS) of Co for the model Co SA@BP and Co-SA/NC@ad-BP.

(E) Bader charge analysis of Co SA@BP and Co-SA/NC@ad-BP.

(F) Schematic of metal-adsorbate interaction change by the metal d-band center (E_d).

As shown in Figures 6 and S20, TEM images show that the electrocatalysts retain a lamellar structure following metal atom modification. Local magnification reveals a significant number of NC present on the ad-BP NSs. EDS mapping images further demonstrate the uniform distribution of Cu, Fe, and Ni across the NSs. HR-TEM images show the characteristic crystalline planes of BP. Additionally, AC-HAADF-STEM imaging shows that Cu, Fe, and Ni coexist as both NC (red circles) and SA (yellow circles) dispersed across the ad-BP NSs (Figures 6B–6E, 6J–6M, and 6R–6U). Based on this, we employed the same statistical approach used for Co-SA/NC@ad-BP to quantitatively analyze the relative proportions of SACs, NCs, and particles in M-SA/NC@ad-BP (M = Cu, Fe, Ni). The results indicate that the BIAES strategy effectively increases the loading of metal species on ad-BP and promotes the synergistic formation of SAs and NCs (Figure S21; Table S5). The normalized K-edge XANES spectra reveal that the adsorption edges of Cu-SA/NC@ad-BP, Fe-SA/NC@ad-BP, and Ni-SA/NC@ad-BP are shifted toward higher energy regions, indicating that their valence states are higher than those of their corresponding metallic foils. EXAFS analysis of Cu-SA/NC@ad-BP and Fe-SA/NC@ad-BP reveals prominent peaks in R-space corresponding to M–P coordination. Fitting results indicate that these features arise from contributions of both SA and NC. For Ni-SA/NC@ad-BP, two peaks within 1–3 Å can likewise be assigned to coexisting SA and NC coordination environments. These results confirm the

Please cite this article in press as: Fan et al., Atomic-level etching enables black phosphorus-based electrocatalysts with tuned high-loading single-atom/nanocluster microdomains, Matter (2026), https://doi.org/10.1016/j.matt.2026.102857

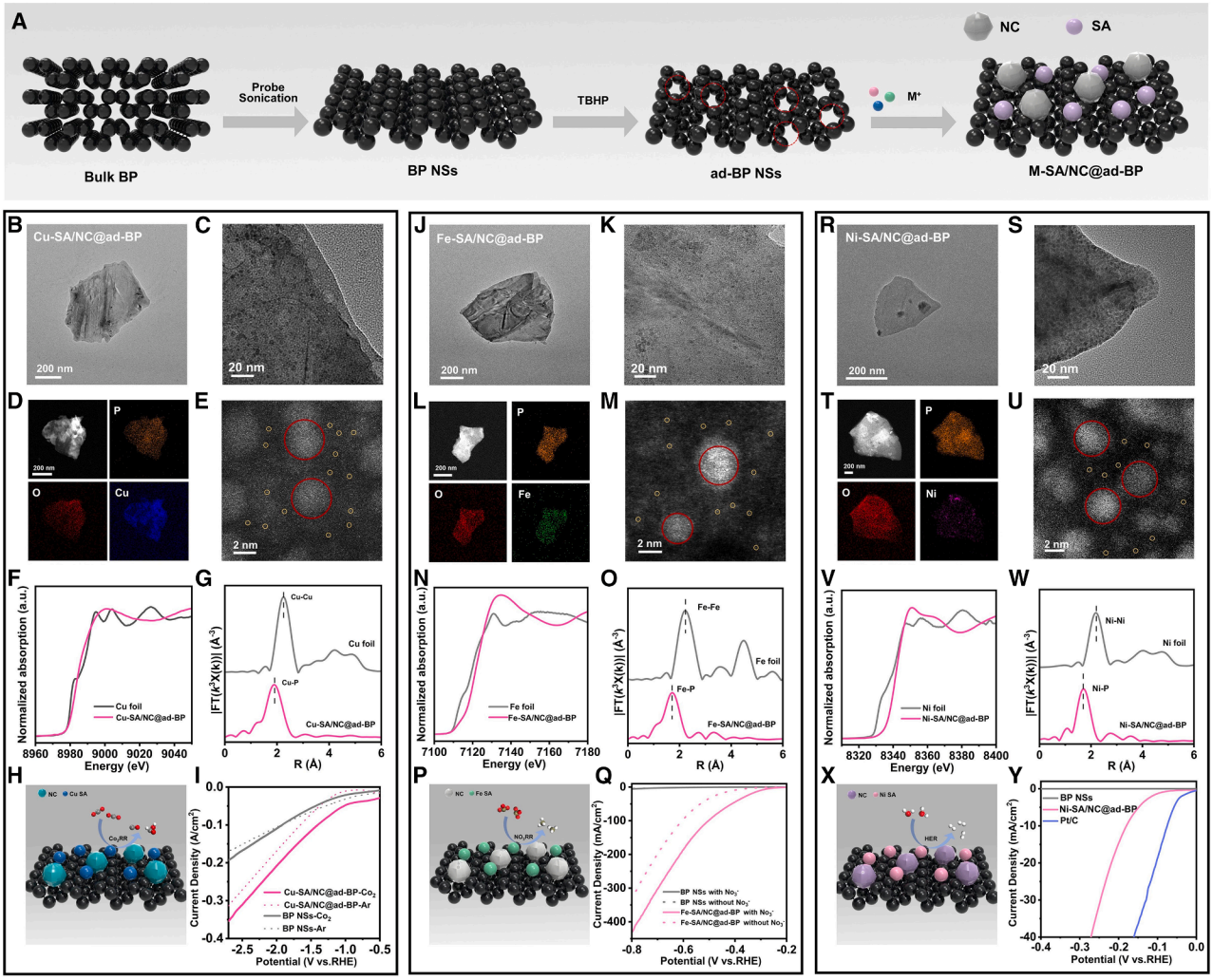

Figure 6. Universal synthesis of M-SA/NC@ad-BP

(A) Illustration of the M-SA/NC@ad-BP synthesis process.

(B and C) TEM images under low and high magnitudes of Cu-SA/NC@ad-BP.

(D) EDS mapping images of Cu-SA/NC@ad-BP, showing the distribution of P, O, and Cu.

(E–G) HAADF-STEM image of the Cu-SA/NC@ad-BP (E). Normalized Cu K-edge XANES spectra (F), Fourier transform k^3-weighted Cu K-edge EXAFS spectra (G) of Cu foil and Cu-SA/NC@ad-BP.

(H) Schematic illustration of Co_2RR process.

(I) LSV curves recorded in CO_2-saturated 0.1 M $KHCO_3$ solution.

(J and K) TEM images under low and high magnitudes of Fe-SA/NC@ad-BP.

(L) EDS mapping images of Fe-SA/NC@ad-BP, showing the distribution of P, O, and Fe.

(M–O) HAADF-STEM image of the Fe-SA/NC@ad-BP (M). Normalized Fe K-edge XANES spectra (N), Fourier transform k^3-weighted Fe K-edge EXAFS spectra (O) of Fe foil and Fe-SA/NC@ad-BP.

(P) Schematic illustration of NO_3RR process.

(Q) LSV polarization curves.

(R and S) TEM images under low and high magnitudes of Ni-SA/NC@ad-BP.

(T) EDS mapping images of Ni-SA/NC@ad-BP, showing the distribution of P, O, and Ni.

(U) HAADF-STEM image of the Ni-SA/NC@ad-BP. Normalized Ni K-edge XANES spectra (V), Fourier transform k^3-weighted Ni K-edge EXAFS spectra (W) of Ni foil and Ni-SA/NC@ad-BP.

(X) Schematic illustration of HER process.

(Y) Polarization curves tested.

Please cite this article in press as: Fan et al., Atomic-level etching enables black phosphorus-based electrocatalysts with tuned high-loading single-atom/nanocluster microdomains, Matter (2026), https://doi.org/10.1016/j.matt.2026.102857

coexistence of SA and NC across all three systems (Figures 6F, 6G, 6N, 6O, 6V, 6W, S22, S23, S24, S25, S26, and S27; Tables S6, S7, and S8). We further evaluated the performance of Cu-SA/NC@ad-BP, Fe-SA/NC@ad-BP, and Ni-SA/NC@ad-BP catalysts for CO_2RR, NO_3RR, and HER, respectively. As shown in Figures 6H and 6I, Cu-SA/NC@ad-BP exhibits significantly enhanced activity for CO_2RR compared to BP NSs, delivering a Faradaic efficiency of 66.7% toward formate (Figure S28; Table S9), indicative of high activity and selectivity. In Figures 6P and 6Q, Fe-SA/NC@ad-BP exhibits higher current densities in NO_3^- containing electrolyte and achieves a Faradaic efficiency of 93.2% for ammonia at −0.7 V, demonstrating its high NO_3RR performance (Figure S29; Table S10).[46] Moreover, Ni-SA/NC@ad-BP achieved excellent performance for HER, requiring an overpotential of only 180 mV to reach a current density of 10 mA cm^{-2} (Figures 6X, 6Y, and S30; Table S11). These results indicate that ad-BP NSs-based SA/NC electrocatalysts constructed via BIAES have broad application prospects in energy catalysis.

Conclusion

In summary, the BIAES strategy introduced here establishes a generalizable approach for constructing high-density and uniformly distributed metal-based SAs and NCs on ad-BP NSs. By exploiting the anchoring and confinement effects of atomic-scale defects, together with the strong electronic coupling between SA/NC species and the support, the resulting M-SA/NC@ad-BP catalysts (M = Co, Cu, Fe, Ni) deliver outstanding performance across diverse electrocatalytic reactions. The BIAES strategy provides a universal approach for the precise engineering of 2D carriers-based SA/NC electrocatalysts, and opens up a new path for optimizing the performance of SA electrocatalysts.

MATERIALS AND METHODS

Chemicals

BP was purchased from Kunming Black Phosphorus Technology Co., Ltd. (Kunming, China). N-methyl pyrrolidone (NMP, 99%), N,N-dimethylformamide (DMF, 99.8%, anhydrous), sodium acetate trihydrate (CH_3COONa, 99%), nickel (II) acetate tetrahydrate ($NiC_4H_6O_4$, 99.9%), copper acetate monohydrate ($C_4H_6CuO_4$, 99.95%), iron (II) acetate ($C_4H_6O_4Fe$, 95%), iridium oxide (IrO_2, 99.9%), and Co (II) acetate tetrahydrate ($C_4H_6CoO_4$, 99.9%) were obtained from Aladdin Reagents. Pt/C was bought from Macklin Reagents. *Tert*-butyl hydroperoxide ($(CH_3)_3COOH$) were bought from Sigma-Aldrich. All the chemicals were used as received without further purification.

Characterization

TEM images, HAADF-STEM images, and EDS spectra were obtained using a FEI Tecnai G2 F20 microscope, operated at an acceleration voltage of 200 kV. Spherical aberration-corrected STEM imaging was performed on a JEM ARM 300F microscope at 200 kV. XRD patterns were recorded on a D/tex Ultima TV system using Cu Kα radiation (λ = 0.15418 nm). Raman scattering measurements were conducted with a LabRAM HR Evolution high-resolution confocal Raman microscope, employing a 532 nm laser as the excitation source. The sample thickness was measured using an MFP-D-SA-DV atomic force microscope. XPS analysis was performed using a Kratos Axis Ultra DLD spectrometer, with all elemental spectra calibrated against the C 1s peak at 284.8 eV. The Co K-edge XAS spectra were collected at the 4B9A beamline of the Beijing Synchrotron Radiation Facility, China, in transmission mode at room temperature. Data processing for XANES was conducted using the Athena program.[47] For EXAFS analysis, data analysis and shell fitting were performed with Artemis.[48,49] The energy shift (ΔE_0) was constrained to be identical for all scattering paths. Wavelet-transformed k^3-weighted EXAFS data were analyzed using the Hama Fortran code, with a radial range of 0–6 Å and k-weighting of 0. The kappa-Morlet wavelet with a value of 10 for kappa and 1 for sigma was selected as the mother wavelet to provide the overall distribution.[50]

Preparation of ad-BP NSs

First, BP NSs were synthesized via ultrasonic liquid-phase exfoliation. In this process, 50 mg of bulk BP was finely ground and dispersed in a solution of NMP at a concentration of 1 mg mL^{-1}. The mixture was then purged with nitrogen for 30 min to eliminate dissolved oxygen. Following sonication, the suspension was centrifuged at 3,000 rpm for 10 min to remove any unexfoliated bulk BP. To further synthesize the ad-BP NSs, the solvent in the BP NSs-containing supernatant was replaced with ultrapure water pre-bubbled with argon for 30 min to eliminate dissolved oxygen. Subsequently, an equal volume of decane containing 5×10^{-4} M *tert*-butyl hydroperoxide was added to the dispersion and stirred gently in the dark for 4 h. The mixture was then centrifuged at 9,000 rpm for 10 min to collect the ad-BP NSs. The resulting precipitate was repeatedly washed with DMF and stored for subsequent use.

Preparation of M-SA/NC@ad-BP

For the synthesis of Co-SA/NC@ad-BP, 1.5 mg of Co (II) acetate tetrahydrate and 3 mg of CH_3COONa were dissolved in 10 mL of ad-BP NSs in DMF. The solution was thoroughly mixed and transferred to a 15 mL Teflon-lined reactor. The reactor was sealed under an argon atmosphere to prevent exposure to oxygen. The reactor was then heated in an oven at 180°C for 4 h. After cooling to room temperature, the solution was centrifuged at 10,000 rpm for 5 min to isolate the product, which was subsequently washed with ethanol. For the synthesis of M-SA/NC@ad-BP (M = Cu, Fe, Ni), the metal precursors were substituted with the corresponding metal acetates, while the remaining procedures were identical to those used for the synthesis of Co-SA/NC@ad-BP.

Statistical analysis of SACs, NCs, and particles

Based on aberration-corrected HAADF-STEM images, SACs are identified as isolated bright spots with intensities significantly higher than the BP background and without discernible aggregation. NCs are defined as Co aggregates smaller than 3 nm, consisting of multiple Co atoms. Particles are assigned to Co species with sizes ≥3 nm and clear structural boundaries.[51] For statistical analysis, at least 50 Co-containing structural units were randomly selected from different regions. The ratio of NCs

to particles was first determined. Combined with locally magnified HAADF-STEM images and size measurements, the number of Co atoms within each structural unit was estimated. These data, together with bulk compositional analysis, were used to calculate the relative proportions of SACs, NCs, and particles.

Preparation of SAC@C

A total of 1.4 mM $Co(NO_3)_2{\cdot}6H_2O$ and 11.2 mM $Zn(NO_3)_2{\cdot}6H_2O$ were dissolved in 123 mL of methanol to obtain a clear solution, referred to as solution A. Separately, 19.7 mM 2-methylimidazole was dissolved in 123 mL of methanol to form solution B. Solutions A and B were then mixed thoroughly and allowed to react at room temperature for 24 h. The resulting precipitate was collected by centrifugation, washed repeatedly with methanol and deionized water, and dried at 80°C overnight. The obtained precursor was subsequently transferred to a tube furnace and heated to 900°C for 2 h under an Ar atmosphere at a rate of 5°C·min^{-1}. After natural cooling to room temperature, the final product was collected and denoted as SAC@C.

Preparation of NC@C

A total of 0.546 g $Co(NO_3)_2{\cdot}6H_2O$ and 0.558 g $Zn(NO_3)_2{\cdot}6H_2O$ were dissolved in 15 mL of methanol to obtain a clear solution. This solution was rapidly added to 15 mL of methanol containing 0.616 g 2-methylimidazole, followed by ultrasonication at room temperature for 10 min. The resulting mixture was transferred to a 50 mL Teflon-lined stainless-steel autoclave and heated at 120°C for 4 h. The precipitate was collected by centrifugation, washed several times with ethanol, and dried under vacuum at 70°C overnight.

The obtained precursor powder was then placed in a tube furnace and heated to 800°C at a rate of 5°C min^{-1} under a N_2 atmosphere, maintained for 3 h, and allowed to cool naturally to room temperature. The resulting product was used directly without further purification.

Electrochemical characterization

The as-prepared catalysts (5 mg) and Nafion solution (40 μL, 5 wt %) were dissolved in 1 mL of ethanol and sonicated for 30 min to form a homogeneous slurry. A volume of 4 μL of this slurry was then loaded onto the surface of a GCE (3 mm in diameter), and the electrode was dried at room temperature. Electrochemical measurements were performed using a CHI 760E electrochemical workstation (CH Instruments, Inc., Shanghai) in a standard three-electrode configuration. A Hg/HgO (1 M KOH) electrode was used as the reference, and a Pt electrode served as the counter electrode. The electrocatalytic performance toward the OER was evaluated by obtaining polarization curves using LSV with a scan rate of 5 mV s^{-1} at room temperature in a 1.0 M KOH solution, with a catalyst loading of 0.28 mg cm^{-2} on the GCE. Measured potentials were converted to the RHE scale using the equation: $E_{RHE} = E_{Hg/HgO} + 0.059\ pH + E^0_{Hg/HgO}$, where $E^0_{Hg/HgO} = 0.098$ V (25°C). EIS was conducted in the frequency range of 0.1 Hz–1,000 kHz with an amplitude of 5 mV. The stability of Co-SA/NC@ad-BP was evaluated by potential cycling between 0.2 and 0.3 V (vs. RHE) at a sweep rate of 100 mV s^{-1} for 1,000 cycles, followed by obtaining LSV polarization curves. All data were presented without iR correction. The electrolyte used was 1.0 M KOH.

Calculation of the turnover frequency

The turnover frequency (TOF) (s^{-1}) was calculated using the following formula[31]

$$TOF = \frac{O_2\ \text{turnovers per Ageo}}{\text{Active sites per Ageo}} = \frac{J \times A}{z \times n \times F},$$

where J is the current density (mA cm^{-2}), A is the geometric area of the electrode (0.071 cm^2), z is the number of electrons transferred (OER is 4), F is Faraday constant (96,485.3 C mol^{-1}), and n is the molar number of active sites.

The O_2 turnover per geometric area (A_{geo}) was obtained from the geometric current density for the LSV curves:

$$TOF = \frac{J \times N_A}{z \times F}.$$

The total mass of the catalyst load (n) is determined using the following formula:

$$n = \frac{m \times N_A}{Mw}.$$

m is the loading mass (mg cm^{-2}), N_A is Avogadro constant (6.02×10^{23}), and Mw is the molar mass (g mol^{-1}).

DFT calculation

DFT calculations were performed using the Dmol3 module in Materials Studio 7.0.[52] The Perdew-Burke-Ernzerhof (PBE) functional within the generalized gradient approximation (GGA) was employed to describe the electronic exchange and correlation effects.[53] During geometry optimization, the convergence thresholds for energy change, maximum force, and maximum displacement were set to 1×10^{-5} Ha, 0.002 Ha Å^{-1}, and 0.005 Å, respectively. The self-consistent field (SCF) tolerance was set to 1×10^{-6} Ha. The Brillouin zone was sampled using a $3 \times 3 \times 1$ Monkhorst-Pack k-point mesh. A 15 Å vacuum layer was introduced along the c-direction, perpendicular to the surface, to prevent periodic interactions. The *d*-band center was determined by averaging the integral of the projected density of states (PDOS) of the *d*-band. The steps involved in the OER of transition metal compounds under alkaline conditions are outlined as follows[54]

$$H_2O + {}^* \rightarrow M^*OH + H^+ + e^-,$$

$$M^*OH \rightarrow M^*O + H^+ + e^-,$$

$$M^*O + H_2O \rightarrow M^*OOH + H^+ + e^-,$$

$$M^*OOH \rightarrow M^* + O_2 + H^+ + e^-.$$

The ΔG of the OER intermediate was calculated using the equation $\Delta G = \Delta E + \Delta ZPE - T\Delta S$, where ΔE represents the reaction energy obtained from DFT calculations, ΔZPE is the zero-point energy, T is the temperature (298.15 K), and ΔS is the entropy change derived from vibrational frequency

calculations.[38] The applied overpotentials were set to 0 and 1.23 V vs. RHE, respectively.

RESOURCE AVAILABILITY

Lead contact

Further information and requests for resources and reagents should be directed to and will be fulfilled by the lead contact, Dan Luo (luodan@binn.cas.cn).

Materials availability

This study did not generate any new reagents. The reagents used here are described in the methods section.

Data and code availability

The data needed to evaluate the conclusions in this work are present in the paper and are available from the corresponding author upon reasonable request.

ACKNOWLEDGMENTS

Y.F. and Z.W. contributed equally to this manuscript. The authors are grateful for the support received from the National Natural Science Foundation of China (52372174, 32401198, 82230030, and T2125003), the National Key Research and Development Program of China (2022YFB3205602), and the Beijing Nova Program Interdisciplinary Cooperation Project (no. 20250484970).

AUTHOR CONTRIBUTIONS

Conceptualization, C.L., Z.L., D.L., and D.W.; methodology, Y.F. and Z.W.; software, Y.F. and Z.W.; investigation, Y.F., Z.W., C.L., and B.G.; visualization, Y.F., Z.W., W.W., S.Z., J.Z., W.L., C.Z., and K.R.; funding acquisition, C.L., Z.L., D.L., and D.W.; project administration, C.L., Z.L., and D.L.; supervision, C.L., Z.L., D.L., and D.W.; writing – original draft, Y.F. and Z.W.; and writing – review and editing, C.L., Z.L., D.L., and D.W.

DECLARATION OF INTERESTS

The authors declare no competing interests.

SUPPLEMENTAL INFORMATION

Supplemental information can be found online at https://doi.org/10.1016/j.matt.2026.102857.

Received: February 5, 2026
Revised: April 8, 2026
Accepted: May 5, 2026

REFERENCES

1. Lin, X., Chen, Z., Li, Z., Yang, B., Zhang, Q., Lv, J., Lei, L., Li, Y., Rodriguez, R.D., and Hou, Y. (2026). Design strategies for dual-atom and multi-atom catalysts: Unlocking synergistic interactions in carbon-based electrocatalysis. Fundam. Res. *6*, 765–789. https://doi.org/10.1016/j.fmre.2025.09.016.
2. Li, Y.H., Zhao, S.N., and Zang, S.Q. (2023). Programmable kernel structures of atomically precise metal nanoclusters for tailoring catalytic properties. Exploration *3*, 20220005. https://doi.org/10.1002/EXP.20220005.
3. Chen, R., Chen, S., Wang, L., and Wang, D. (2024). Nanoscale metal particle modified single-atom catalyst: synthesis, characterization, and application. Adv. Mater. *36*, 2304713. https://doi.org/10.1002/adma.202304713.
4. Zhang, J., Huang, Q.A., Wang, J., Wang, J., Zhang, J., and Zhao, Y. (2020). Supported dual-atom catalysts: Preparation, characterization, and potential applications. Chin. J. Catal. *41*, 783–798. https://doi.org/10.1016/S1872-2067(20)63536-7.
5. Hou, G.-L., and Janssens, E. (2026). Supported and isolated metal atoms and clusters as models for understanding the hydrogen economy. Fundam. Res. *6*, 201–211. https://doi.org/10.1016/j.fmre.2023.10.011.
6. Ye, T.N., Xiao, Z., Li, J., Gong, Y., Abe, H., Niwa, Y., Sasase, M., Kitano, M., and Hosono, H. (2020). Stable single platinum atoms trapped in sub-nanometer cavities in $12CaO{\cdot}7Al_2O_3$ for chemoselective hydrogenation of nitroarenes. Nat. Commun. *11*, 1020. https://doi.org/10.1038/s41467-019-14216-9.
7. Ren, Y., Tang, Y., Zhang, L., Liu, X., Li, L., Miao, S., Sheng Su, D., Wang, A., Li, J., and Zhang, T. (2019). Unraveling the coordination structure-performance relationship in Pt_1/Fe_2O_3 single-atom catalyst. Nat. Commun. *10*, 4500. https://doi.org/10.1038/s41467-019-12459-0.
8. Zhou, W., Huang, Y., Cai, H., Wang, T., Li, H., Zhang, C., Zhao, L., Chen, L., Liao, M., Tang, Z., et al. (2025). A strongly coupled cluster heterostructure with Pt-N-Mo bonding for durable and efficient H(2) evolution in anion-exchange membrane water electrolyzers. Nano-Micro Lett. *17*, 296. https://doi.org/10.1007/s40820-025-01798-x.
9. Du, Y., He, Z., Chen, C., Guo, F., Ren, F., Wang, P., Ai, Y., and Liu, P. (2025). Pathogenesis-Guided Nanozymes: From Design to Therapy for Gastrointestinal Inflammation. MedMat. https://doi.org/10.1097/mm9.0000000000000037.
10. Gloag, L., Somerville, S.V., Gooding, J.J., and Tilley, R.D. (2024). Co-catalytic metal-support interactions in single-atom electrocatalysts. Nat. Rev. Mater. *9*, 173–189. https://doi.org/10.1038/s41578-023-00633-2.
11. Guo, Y., Li, J., Dou, R., Ye, H., and Gu, C. (2026). Quantum defects in two-dimensional van der Waals materials. Fundam. Res. *6*, 126–140. https://doi.org/10.1016/j.fmre.2024.01.019.
12. Kundu, J., Kwon, T., Lee, K., and Choi, S.I. (2024). Exploration of metal-free 2D electrocatalysts toward the oxygen electroreduction. Exploration *4*, 20220174. https://doi.org/10.1002/EXP.20220174.
13. Zhao, J., Chen, Z., Liu, S., Li, P., Yu, S., Ling, D., and Li, F. (2024). Nano-bio interactions between 2D nanomaterials and mononuclear phagocyte system cells. BMEMat *2*, e12066. https://doi.org/10.1002/bmm2.12066.
14. Zhang, F., Liu, W., Hao, Z., Lu, H., Liu, J., Pang, H., Zhang, R., Li, X., Wang, Z., and Zhang, L. (2025). Defect-engineered iron single-site catalysts with tailored atomic coordination for enhanced mild photothermal therapy via triad modulation of apoptosis and ferroptosis. BMEMat *4*, e70051. https://doi.org/10.1002/bmm2.70051.
15. Zhou, L., Li, M., Wang, W., Wang, C., Yang, H., and Cao, Y. (2022). Edge engineering in chemically active two-dimensional materials. Nano Res. *15*, 9890–9905. https://doi.org/10.1007/s12274-022-4320-8.
16. Ying, Y., Fan, K., Lin, Z., and Huang, H. (2025). Facing the "cutting edge:" Edge site engineering on 2D materials for electrocatalysis and photocatalysis. Adv. Mater. *37*, 2418757. https://doi.org/10.1002/adma.202418757.
17. Gupta, A., Ndugire, W., Liu, L., Chakraborty, S., Abdelaziz, M., Rainboth, D., and Rotello, V.M. (2024). Bioorthogonal catalysis for antimicrobial therapy. MedMat *1*, 2–5. https://doi.org/10.1097/mm9.0000000000000001.
18. Zhang, Q., Wang, J.-a., Yu, Q., Li, Q., Fan, R., Li, C., Fan, Y., Zhao, C., Cheng, W., Ji, P., et al. (2024). Metal/MXene composites via in situ reduction. Nat. Synth. *4*, 252–261. https://doi.org/10.1038/s44160-024-00660-z.
19. Kang, J., Wood, J.D., Wells, S.A., Lee, J.H., Liu, X., Chen, K.S., and Hersam, M.C. (2015). Solvent exfoliation of electronic-grade, two-dimensional black phosphorus. ACS Nano *9*, 3596–3604. https://doi.org/10.1021/acsnano.5b01143.
20. Zhou, Q., Chen, Q., Tong, Y., and Wang, J. (2016). Light-induced ambient degradation of few-layer black phosphorus: mechanism and protection. Angew. Chem. Int. Ed. *55*, 11437–11441. https://doi.org/10.1002/anie.201605168.
21. Hao, Y., Hung, S.F., Zeng, W.J., Wang, Y., Zhang, C., Kuo, C.H., Wang, L., Zhao, S., Zhang, Y., Chen, H.Y., and Peng, S. (2023). Switching the oxygen

evolution mechanism on atomically dispersed Ru for enhanced acidic reaction kinetics. J. Am. Chem. Soc. *145*, 23659–23669. https://doi.org/10.1021/jacs.3c07777.

22. Zhang, J.Y., Xia, C., Wang, H.F., and Tang, C. (2022). Recent advances in electrocatalytic oxygen reduction for on-site hydrogen peroxide synthesis in acidic media. J. Energy Chem. *67*, 432–450. https://doi.org/10.1016/j.jechem.2021.10.013.

23. Li, W., Wang, Z., Zhao, F., Li, M., Gao, X., Zhao, Y., Wang, J., Zhou, J., Hu, Y., Xiao, Q., et al. (2020). Phosphorene degradation: visualization and quantification of nanoscale phase evolution by scanning transmission X-ray microscopy. Chem. Mater. *32*, 1272–1280. https://doi.org/10.1021/acs.chemmater.9b04811.

24. Duan, J., Chen, S., Ortíz-Ledón, C.A., Jaroniec, M., and Qiao, S.Z. (2020). Phosphorus vacancies that boost electrocatalytic hydrogen evolution by two orders of magnitude. Angew. Chem. Int. Ed. *59*, 8181–8186. https://doi.org/10.1002/anie.201914967.

25. Li, S., Geng, Z., Wang, X., Ren, X., Liu, J., Hou, X., Sun, Y., Zhang, W., Huang, K., and Feng, S. (2020). Optimizing the surface state of cobalt-iron bimetallic phosphide regulating phosphorus vacancies. Chem. Commun. *56*, 2602–2605. https://doi.org/10.1039/c9cc09741d.

26. Wang, J., Liu, D., Huang, H., Yang, N., Yu, B., Wen, M., Wang, X., Chu, P.K., and Yu, X.F. (2018). In-Plane Black Phosphorus/Dicobalt Phosphide Heterostructure for Efficient Electrocatalysis. Angew. Chem. Int. Ed. *57*, 2600–2604. https://doi.org/10.1002/anie.201710859.

27. Wang, X., Gao, R., Fan, G., Guo, Y., Han, C., Gao, Y., Shen, A., Wu, L., and Gu, X. (2025). Dual defects-induced iron single atoms immobilized in metal-organic framework-derived hollow BiOBr microtubes for low-barrier photocatalytic nitrogen reduction. Angew. Chem. Int. Ed. *64*, e202501297. https://doi.org/10.1002/anie.202501297.

28. Shi, F., Geng, Z., Huang, K., Liang, Q., Zhang, Y., Sun, Y., Cao, J., and Feng, S. (2018). Cobalt nanoparticles/black phosphorus nanosheets: an efficient catalyst for electrochemical oxygen evolution. Adv. Sci. *5*, 1800575. https://doi.org/10.1002/advs.201800575.

29. Gao, Y., Qian, S., Wang, H., Yuan, W., Fan, Y., Cheng, N., Xue, H., Jiang, T., and Tian, J. (2023). Boron-doping on the surface mediated low-valence Co centers in cobalt phosphide for improved electrocatalytic hydrogen evolution. Appl. Catal. B Environ. *320*, 122014. https://doi.org/10.1016/j.apcatb.2022.122014.

30. Zhou, H., Zheng, M., and Pang, H. (2021). Synthesis of hollow amorphous cobalt phosphide-cobalt oxide composite with interconnected pores for oxygen evolution reaction. Chem. Eng. J. *416*, 127884. https://doi.org/10.1016/j.cej.2020.127884.

31. Guo, B., Wang, Z., Zheng, L., Mo, G., Zhou, H., and Luo, D. (2024). Confined cobalt single-atom catalysts with strong electronic metal-support interactions based on a biomimetic self-assembly strategy. Carbon Energy *6*, e554. https://doi.org/10.1002/cey2.554.

32. Chen, H., Gao, Y., Du, J., Hao, R., Wu, X., Wang, L., and Wu, Z. (2026). Bridging cobalt single atom satellite and nanoparticle synergies for efficient low-concentration NO electroreduction to ammonia. ACS Nano *20*, 2323–2336. https://doi.org/10.1021/acsnano.5c18397.

33. Duan, W., Chen, Y., Zhu, Y., Tian, L., Zheng, W., Fu, H., Chen, J.L., Lin, Y.J., Lam, J.C.H., Lei, Y., and Feng, C. (2025). Synergistic effects of Co single atoms and Co nanoparticles for electrocatalytic nitrate-to-ammonium conversion in strongly acidic wastewater. Appl. Catal. B Environ. *363*, 124812. https://doi.org/10.1016/j.apcatb.2024.124812.

34. Wei, X., Zhang, S., Lv, X., Dai, S., Wang, H., and Huang, M. (2024). Local-reconstruction enables cobalt phosphide array with bifunctional hydrogen evolution and hydrazine oxidation. Appl. Catal. B Environ. *345*, 123661. https://doi.org/10.1016/j.apcatb.2023.123661.

35. Fei, H., Dong, J., Arellano-Jiménez, M.J., Ye, G., Dong Kim, N., Samuel, E.L.G., Peng, Z., Zhu, Z., Qin, F., Bao, J., et al. (2015). Atomic cobalt on nitrogen-doped graphene for hydrogen generation. Nat. Commun. *6*, 8668. https://doi.org/10.1038/ncomms9668.

36. Zhou, K.L., Wang, Z., Han, C.B., Ke, X., Wang, C., Jin, Y., Zhang, Q., Liu, J., Wang, H., and Yan, H. (2021). Platinum single-atom catalyst coupled with transition metal/metal oxide heterostructure for accelerating alkaline hydrogen evolution reaction. Nat. Commun. *12*, 3783. https://doi.org/10.1038/s41467-021-24079-8.

37. Liu, Y., Liu, X., Jadhav, A.R., Yang, T., Hwang, Y., Wang, H., Wang, L., Luo, Y., Kumar, A., Lee, J., et al. (2022). Unraveling the function of metal–amorphous support interactions in single-atom electrocatalytic hydrogen evolution. Angew. Chem. Int. Ed. *61*, e202114160. https://doi.org/10.1002/anie.202114160.

38. Zhu, Y., Wang, J., Koketsu, T., Kroschel, M., Chen, J.M., Hsu, S.Y., Henkelman, G., Hu, Z., Strasser, P., and Ma, J. (2022). Iridium single atoms incorporated in Co_3O_4 efficiently catalyze the oxygen evolution in acidic conditions. Nat. Commun. *13*, 7754. https://doi.org/10.1038/s41467-022-35426-8.

39. Guan, D., Zhou, J., Huang, Y.C., Dong, C.L., Wang, J.Q., Zhou, W., and Shao, Z. (2019). Screening highly active perovskites for hydrogen-evolving reaction via unifying ionic electronegativity descriptor. Nat. Commun. *10*, 3755. https://doi.org/10.1038/s41467-019-11847-w.

40. Li, G., Jang, H., Liu, S., Li, Z., Kim, M.G., Qin, Q., Liu, X., and Cho, J. (2022). The synergistic effect of Hf-O-Ru bonds and oxygen vacancies in Ru/HfO2 for enhanced hydrogen evolution. Nat. Commun. *13*, 1270. https://doi.org/10.1038/s41467-022-28947-9.

41. Zhao, X., and Liu, Y. (2021). Origin of selective production of hydrogen peroxide by electrochemical oxygen reduction. J. Am. Chem. Soc. *143*, 9423–9428. https://doi.org/10.1021/jacs.1c02186.

42. Mei, J., He, T., Bai, J., Qi, D., Du, A., Liao, T., Ayoko, G.A., Yamauchi, Y., Sun, L., and Sun, Z. (2021). Surface-dependent intermediate adsorption modulation on iridium-modified black phosphorus electrocatalysts for efficient pH-universal water splitting. Adv. Mater. *33*, 2104638. https://doi.org/10.1002/adma.202104638.

43. Liu, T., Wang, Y., and Li, Y. (2022). Two-dimensional organometallic frameworks with pyridinic single-metal-atom sites for bifunctional ORR/OER. Adv. Funct. Mater. *32*, 2207110. https://doi.org/10.1002/adfm.202207110.

44. Liu, J., Guo, Y., Fu, X.Z., Luo, J.L., and Zhi, C. (2023). Strengthening absorption ability of Co-N-C as efficient bifunctional oxygen catalyst by modulating the d band center using MoC. Green Energy Environ. *8*, 459–469. https://doi.org/10.1016/j.gee.2021.05.008.

45. Wang, L., Ma, M., Zhang, C., Chang, H.H., Zhang, Y., Li, L., Chen, H.Y., and Peng, S. (2024). Manipulating the microenvironment of single atoms by switching support crystallinity for industrial hydrogen evolution. Angew. Chem. Int. Ed. *63*, e202317220. https://doi.org/10.1002/anie.202317220.

46. Yang, W., Chang, Z., Yu, X., Shen, R., Wang, L., Cui, X., and Shi, J. (2025). Triple regulations via Fe redox boosting nitrate reduction to ammonia at industrial current densities. Angew. Chem. Int. Ed. *64*, e202415300. https://doi.org/10.1002/anie.202415300.

47. Ravel, B., and Newville, M. (2005). ATHENA, ARTEMIS, HEPHAESTUS: data analysis for X-ray absorption spectroscopy using IFEFFIT. J. Synchrotron Radiat. *12*, 537–541. https://doi.org/10.1107/S0909049505012719.

48. Newville, M. (2001). EXAFS analysis using FEFF and FEFFIT. J. Synchrotron Radiat. *8*, 96–100. https://doi.org/10.1107/S0909049500016290.

49. Rehr, J.J., and Albers, R.C. (2000). Theoretical approaches to x-ray absorption fine structure. Rev. Mod. Phys. *72*, 621–654. https://doi.org/10.1103/RevModPhys.72.621.

50. Liu, Y.P., Sheng, W.F., and Wu, Z.H. (2021). Synchrotron radiation and its applications in inorganic materials. J. Inorg. Mater. *36*, 901–918. https://doi.org/10.15541/jim20200703.

51. Yau, S.H., Varnavski, O., and Goodson, T. (2013). An ultrafast look at Au nanoclusters. Acc. Chem. Res. *46*, 1506–1516. https://doi.org/10.1021/ar300280w.

52. Delley, B. (2000). From molecules to solids with the DMol3 approach. J. Chem. Phys. *113*, 7756–7764. https://doi.org/10.1063/1.1316015.

53. Perdew, J.P., Burke, K., and Ernzerhof, M. (1996). Generalized gradient approximation made simple. Phys. Rev. Lett. *77*, 3865–3868. https://doi.org/10.1103/PhysRevLett.77.3865.

54. Peng, L., Yang, N., Yang, Y., Wang, Q., Xie, X., Sun-Waterhouse, D., Shang, L., Zhang, T., and Waterhouse, G.I.N. (2021). Atomic cation-vacancy engineering of NiFe-layered double hydroxides for improved activity and stability towards the oxygen evolution reaction. Angew. Chem. Int. Ed. *60*, 24612–24619. https://doi.org/10.1002/anie.202109938.